Article

A rolling-mode triboelectric nanogenerator with multi-tunnel grating electrodes and opposite-charge-enhancement for wave energy harvesting

Yawei Wang[1,2,4], Hengxu Du[2,4], Hengyi Yang[2,4], Ziyue Xi[2,4], Cong Zhao[2], Zian Qian[2], Xinyuan Chuai[3], Xuzhang Peng[1], Hongyong Yu[2], Yu Zhang[2], Xin Li[3], Guobiao Hu ●[1] ✉, Hao Wang[2] ✉ & Minyi Xu ●[2] ✉

In light of the crucial role of marine ecosystems and the escalating environmental conservation challenges, it is essential to conduct marine monitoring to help implement targeted environmental protection measures efficiently. Energy harvesting technologies, particularly triboelectric nanogenerators (TENGs), have great potential for prolonging the lifespan and enhancing the reliability of sensors in remote areas. However, the high internal resistance, low current, and friction-induced abrasion issues of TENGs limit their performance in practical applications. This work presents a rolling mode triboelectric nanogenerator that utilizes multi-tunnel grating electrodes and the opposite-charge-enhancement mechanism to harvest wave energy efficiently. The device achieves significant instantaneous and root mean square power density of 185.4 W/(m³·Hz) and 10.92 W/(m³·Hz), respectively. By utilizing stacked devices and an exclusively designed power management module, a self-powered ocean sensing system including computing and long-range wireless communication (0.8 km) capabilities was developed. Laboratory and in-situ ocean tests were conducted to assess and validate the system. This work offers a potential solution for the challenging deployment of marine self-powered sensing nodes.

More than 95% of the ocean is unexplored by humans, though it is crucial to the climate system, harbors many undiscovered species, and governs the global weather pattern[1]. The urgency for ocean exploration is escalating because of global population growth and the pressing need for resources. However, significant threats such as marine pollution and climate change present significant challenges to the marine environment and resources[2]. Therefore, deploying real-time and long-term monitoring technologies is imperative for ensuring ocean sustainability[3,4]. Nevertheless, the harsh and expansive nature of the oceanic environment often restricts the lifespan and deployment scope of monitoring equipment with heavy reliance on batteries and/or cord power supplies. Harnessing in-situ energy from the marine environment to energize ocean observation nodes presents a viable solution to overcome these limitations[5–7]. Many designs, therefore,

[1]Thrust of Internet of Things, The Hong Kong University of Science and Technology (Guangzhou), Guangzhou, China. [2]State Key Laboratory of Maritime Technology and Safety, Marine Engineering College, Dalian Maritime University, Dalian, China. [3]Guangzhou Institute of Technology, Xidian University, Guangzhou, China. [4]These authors contributed equally: Yawei Wang, Hengxu Du, Hengyi Yang, Ziyue Xi. ✉e-mail: guobiaohu@hkust-gz.edu.cn; hao8901@dlmu.edu.cn; xuminyi@dlmu.edu.cn

have been proposed to convert marine energy into electricity through different transduction mechanisms, including electromagnetic[8], piezoelectric[9,10], and triboelectric[11–13]. Triboelectric nanogenerators (TENGs) possess characteristics such as simple structure, magnet-free, lightweight, and robustness based on the principle of triboelectrification and electrostatic induction. Studies have pointed out that TENGs are more suitable for harvesting high-entropy kinetic energy and powering milli-watt electronics than other technologies[14].

The utilization of TENGs for harvesting blue energy has attracted considerable interest[15–18]. Over the last decade, a variety of prototypes have been developed and can be broadly classified into two primary categories: open and enclosed configurations. Open-type TENGs are based on the triboelectrification between solid and liquid[19,20]. These harvesters have simple structures and are lightweight. Nonetheless, the durability of the contact materials in open-type TENGs is significantly reduced due to seawater's corrosive effect. Enclosed-type TENG scavenges blue energy through the relative motion generated by inertia[21,22]. Equipping TENGs with a protective casing can shield them from harsh ocean conditions, thereby boosting their outputs and extending their service lifespans[23–26]. Employing rolling balls as inertial bodies is esteemed as an ideal scheme in this field[27,28]. The low friction and effortless activation characteristic of the rolling balls contribute to significantly enhancing durability, seamless integration, and superior output performance of the rolling-mode TENGs[29,30].

In 2015, Wang et al.[31] proposed a free-standing TENG based on a rolling structure (RF-TENG), for harvesting wave energy. The enclosed structure and the rolling mode facilitated high charge transfer and low friction. Zhang et al.[26] designed a sea-snake structure-inspired TENG (SS-TENG) for ocean energy harvesting. Unlike the RF-TENG, which features a spherical configuration, the SS-TENG was engineered with a hexahedral architecture. This design choice allows for additional dielectric balls, facilitating a greater power output. Recent advancements in the field have enhanced the SS-TENG through materials selection[21], electrode design[25,32–34], and building harvester networks[35], promoting it toward practical applications in the ocean. While it has been proven that TENGs, particularly those in rolling mode, can be effectively driven by wave to generate substantial voltage output, the prevalent low-frequency wave dynamics in marine environments typically lead them to produce very limited current outputs (<5 μA) at optimal resistances reaching giga-Ohms (GΩ). This limitation poses significant challenges for directly employing such TENGs to power electronic devices in the marine environment. Grating electrodes are employed to boost current output and decrease internal resistance by accelerating charge transfer[36], typically in conjunction with sliding mode TENGs[3] and frequency up-conversion strategies (FUC)[24]. However, the inherent sliding friction in sliding mode TENGs significantly deteriorates their output performance and durability[37]. On the other hand, although the FUC strategy can optimize the performance of piezoelectric and electromagnetic generators, it diminishes the efficacy of TENGs in low-frequency applications.

In this work, a rolling-mode triboelectric nanogenerator (MO-TENG) is designed and proposed. It utilizes multi-tunnel grating electrodes and the opposite-charge-enhancement mechanism to harvest wave energy efficiently, as illustrated in Fig. 1a–d. These strategies improve TENGs' performance, leading to an instantaneous power density of 185.4 W/(m³·Hz) and a root mean square (RMS) power density of 10.92 W/(m³·Hz). A power management module (PMM) is designed to optimize the capacitor charging performance, resulting in an -150-fold increase in stored energy. Furthermore, a self-powered ocean sensing (SOS) system with ultra-low power consumption and cold-start capability has been developed to enable wireless self-powered sensing. Notably, a buoy equipped with stacked MO-TENG units was tested both in the laboratory and in the real ocean. This smart buoy successfully realized self-powered water quality monitoring and wireless communication tasks, demonstrating significant potential for

practical deployment. Overall, the design methodology presented in this work could notably improve the performance of rolling-mode triboelectric nanogenerators, offering a reliable solution for their use within the marine Internet of Things (IoT) domain.

Results

Configuration and working mechanism

Figure 1a shows the 3D exploration diagram of the MO-TENG, which consists of two substrates, two baffles, grating electrodes, PTFE balls, and Nylon balls. The substrates and baffles are fabricated via fused deposition modeling (FDM) 3D printing technology, using polylactic acid (PLA) as the printing material. Other components of the TENG are enclosed in the housing composed of the two substrates and baffles. Dielectric (PTFE and Nylon) balls serve as inertial bodies that can roll back and forth in the housing tunnel. The rolling-mode design, illustrated in Fig. 1b, ensures that the TENG can be easily activated and also offers the benefits of low friction and improved durability. Copper (Cu) foil tapes are equidistantly attached to the substrates to serve as the electrodes and the electrification material. This approach incorporates multi-tunnel and grating electrodes to enhance the electrostatic induction and the current output, as illustrated in Fig. 1c, d[36]. Moreover, PTFE and Nylon balls with opposite-charge polarization are packed and arranged in the multi-tunnel structure, leading to a ternary electrification architecture (PTFE, Cu, and Nylon), as illustrated in Fig. 1e. As the opposite-charge-enhancement is introduced in the rolling mode, the output of the MO-TENG is significantly enhanced. Figure 1f illustrates a substantial enhancement of the MO-TENG's performance, showcasing a transferred charge of 319.1 nC and an output current of 16 μA. Compared with the flat structure TENG (F-TENG)[33] and multi-tunnel TENG (M-TENG)[32], the MO-TENG exhibits a 7-fold and 2.3-fold increase in transferred charge and a 51.6-fold and 14.95-fold increase in current output, respectively. Referring to previous studies of rolling-mode TENGs, the MO-TENG has a small internal resistance and can produce a much larger peak power density, as shown in Fig. 1g[21,25,30,33–35,38,39]. The blueprints of this device in ocean applications are depicted in Fig. 1h. Integrated with buoys, MO-TENGs can be able to convert chaotic, low-frequency, high-entropy wave energy into electricity, powering light-emitting diodes (LEDs), sensors, and communication modules serving marine beacons, farms, and contaminant alarms.

The proposed MO-TENG can boost the output by utilizing multi-tunnel grating electrodes. This is because the multi-tunnel strategy increases the effective electrode area during the balls' rolling process, compared with the flat electrode structure[21,26,33,34]. Moreover, the multiple isolated channels restrict the movements of the inertial balls, allowing them to move between electrodes in a more regulated manner rather than being highly random[21,25]. Prior to a thorough experiment on the MO-TENG to evaluate its electric characteristics, the choices of the design parameters of the MO-TENG are first explained in Supplementary Note 1. In this study, dielectric balls with a diameter of 12.7 mm and multi-tunnel grating electrodes with a diameter of 13.5 mm are used for further experiments. Figure 2a–g compares the electrode configurations of the F-TENG, the M-TENG, and the MO-TENG to elaborate on their differences. In this study, the housing of the rolling-mode TENG is conceptually simplified to a hexahedral shape, as depicted in Fig. 2a. The length, width, and height are L_1, L_2, and H, respectively. The $X–Z$ and $Y–Z$ views of the F-TENG, the M-TENG, and the MO-TENG are shown in Fig. 2b–g, respectively. The substrate thickness is denoted by δ_1, the thickness of the Cu film is δ_2, and the diameter of the inertial balls is d. Note that for the M-TENG, the spacing between each tunnel is δ_3.

To make a fair comparison, we assume that the numbers of PTFE balls in three kinds of TENGs are the same, with n_1 in the X direction and n_2 in the Y direction. Furthermore, the distance between two electrodes is all set as g. According to the geometric relation illustrated in the
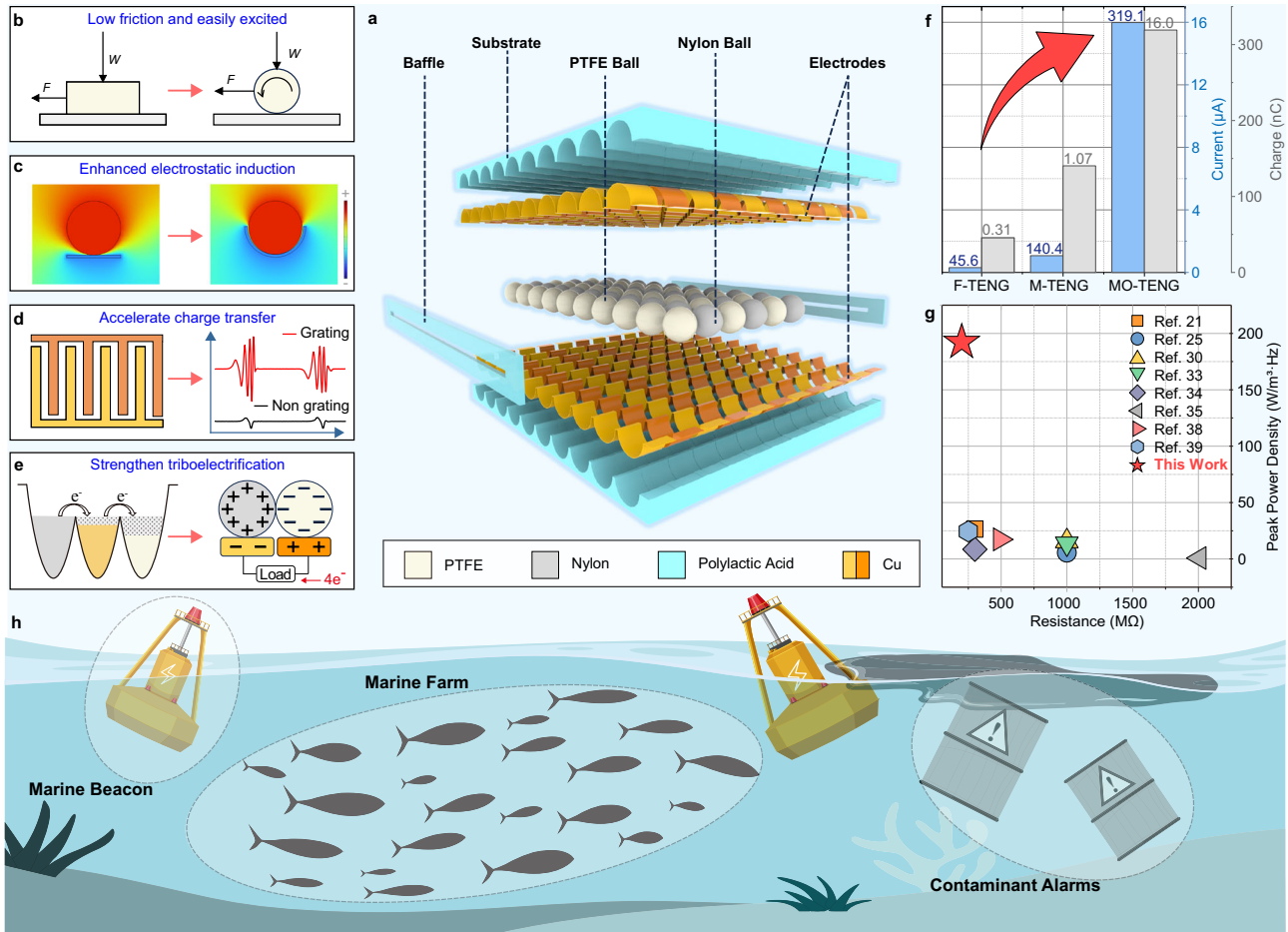
Fig. 1 | Design and boosting strategies of the MO-TENG. a Structure scheme of the MO-TENG. The rolling mode (**b**), tunnel-shaped electrode (**c**), grating electrodes (**d**), and opposite-charge enhancement strategies (**e**) adopted in this work. **f** Comparison of the transferred charge and current generated by the F-TENG, M-TENG, and MO-TENG. **g** Comparison of the peak power and optimal resistance of the MO-TENG with other designs[21,25,30,33–35,38,39]. **h** Potential application scenarios of the proposed MO-TENG.

figures, the parameters of the housing of the F-TENG, the M-TENG, and the MO-TENG can be calculated as follows:

$$
\begin{cases}
L_{1,\text{F--TENG}} = n_1 d + \delta_c \\
L_{2,\text{F--TENG}} = 2n_2 d + g \\
H_{\text{F--TENG}} = d + 2(\delta_1 + \delta_2)
\end{cases}
\tag{1}
$$

$$
\begin{cases}
L_{1,\text{M--TENG}} = n_1 (d + 2\delta_2 + \delta_3) \\
L_{2,\text{M--TENG}} = 2n_2 d + g \\
H_{\text{M--TENG}} = d + 2(\delta_1 + \delta_2)
\end{cases}
\tag{2}
$$

$$
\begin{cases}
L_{1,\text{MO--TENG}} = n_1 (d + 2\delta_2 + \delta_3) \\
L_{2,\text{MO--TENG}} = 2n_2 (d + g) \\
H_{\text{MO--TENG}} = d + 2(\delta_1 + \delta_2)
\end{cases}
\tag{3}
$$

where δ_2 and δ_3 represent the differences in L_1 and L_2 between the F-TENG and the M-TENG, respectively. Assessing the spacing between dielectric balls in the X–Y plane presents a challenge. To address this, the parameter δ_c is introduced to quantify the total gap distance along the X direction in the F-TENG, excluding the space occupied by dielectric balls. Furthermore, from Eqs. (2, 3), one can find that the change of L_2 between the M-TENG and the MO-TENG originates from the presence of multiple gaps in multi-tunnel grating electrodes. Limited by the 3D printer, the minimum δ_3 that can be set is 1.5 mm,

and g is 1.7 mm. The thickness of the used Cu film (δ_2) is 0.15 mm, and the inertial ball's diameter d is 12.7 mm. We set $L_1 = L_2 = 150$ mm for the convenience of manufacturing and assembly. Substituting these values into Eqs. (1–3) yields (n_1, n_2) for the F-TENG, the M-TENG, and the MO-TENG as (11.8110, 5.8386), (10.3448, 5.8386), and (10.3448, 5.2083), respectively. To ensure a fair comparison, the three TENGs should have the same number of balls. As the numbers of balls are integers, n_1 is set at 10 and n_2 at 6 for the subsequent analysis. Considering $n_2 = 6$, the multi-tunnel grating electrode with 12 segments is determined, as discussed in Supplementary Note 1. The electrode areas in the three TENGs are formulated by:

$$
\begin{cases}
S_{\text{F--TENG}} = 2L_1 L_2 - 2gL_1 \\
S_{\text{M--TENG}} = n_1 \pi d (L_2 - g) \\
S_{\text{MO--TENG}} = n_1 \pi d L_2 - 2n_1 n_2 \pi dg
\end{cases}
\tag{4}
$$

substituting the design values into Eq. (4) yields $S_{\text{F--TENG}} = 44{,}490$ mm², $S_{\text{M--TENG}} \approx 59{,}167$ mm², and $S_{\text{MO--TENG}} \approx 51{,}708$ mm², indicating that the effective electrode areas of the M-TENG and the MO-TENG are enlarged by 33% and 16%, respectively, compared with the F-TENG. The enlargement of the electrode area contributes to the improvement of the performance of the M-TENGs[25,32].

Figure S1 shows the photograph of the F-TENG and the M-TENG, housing the same number of PTFE dielectric balls. The short current transfer charge (Q_{sc}) of the two TENGs is evaluated and compared in Fig. S2. The result shows that the transferred charge amount increased
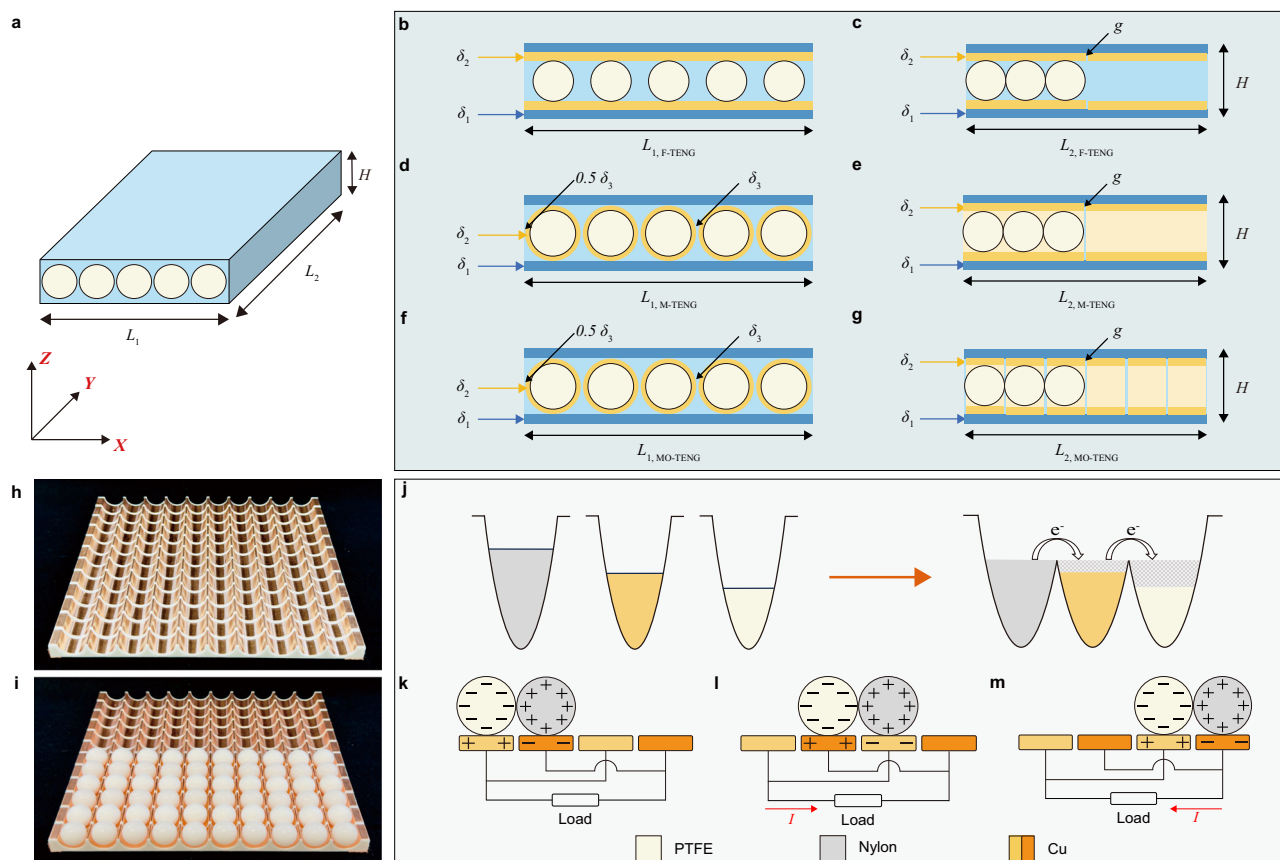
Fig. 2 | Design and working principle of the MO-TENG. a Dimension parameters of the rolling-mode TENG model. *X–Z* and *Y–Z* views of the F-TENG (**b**, **c**), M-TENG (**d**, **e**), and MO-TENG (**f**, **g**). Photograph of the multi-tunnel grating electrodes without dielectric balls (**h**) and with dielectric balls (**i**). **j** Diagram of electrons transition between the ternary triboelectrification materials. **k–m** Working principle of the MO-TENG.

by over twofold with the use of the multi-tunnel structure. The prototyped multi-tunnel grating electrode structures without/with dielectric balls are shown in Fig. 2h, i, respectively. There are two sets of electrode networks with 12 segments in complementary patterns. Fine grooves separate the neighboring tunnels. PTFE and Nylon balls with opposite-charge affinities serve as the inertial bodies that roll in the MO-TENG and also the materials that incur triboelectrification. The triboelectrification that occurs between two materials, such as PTFE and Nylon, is illustrated in Fig. S3, utilizing the surface state model[40]. Together with the electrode material (Cu), the three materials constitute a ternary triboelectrification layer, and the electron cloud potential-well models are shown in Fig. 2j. Due to the different charge affinities of the three materials, the electrons will migrate from higher orbits to empty orbits when they get into contact until the potential-well depths are balanced. According to the triboelectric series[41], the charge affinities of the three materials are ranked as PTFE > Cu > Nylon, implying that the electrons transfer from Nylon to Cu and PTFE in the contact interface. Existing research suggests that implementing a ternary electrification layered architecture can significantly improve triboelectrification when compared to a binary counterpart[37,42], leading to an augmented output performance.

In addition, this strategy can also affect the electrostatic induction process through an opposite-charge-enhancement mechanism, as depicted in Fig. S4. It illustrates that the induced transfer charge between two electrodes is doubled owing to the presence of two distinct types of balls. The working principle of the MO-TENG resembles the free-standing mode TENG[43], with the movable part's length being half of the stator's length, as shown in Fig. 2k–m. Assuming the triboelectrification process is saturated, the PTFE and Nylon balls, respectively, carry negative and positive charges. Suppose Fig. 2k depicts the initial states of the balls. When they roll toward the right (Fig. 2l), a conduction current flowing rightward is produced due to the variation of the displacement current. As the ball continues to roll toward Fig. 2m, a leftward current is generated until the ball stops. To further substantiate the proposed mechanism, the potential distributions of the MO-TENG with two and six dielectric balls were simulated using COMSOL (Figs. S5, 6). It should be noted that the results were obtained under open-circuit conditions. A completed and assembled MO-TENG is shown in Fig. S7, and the dimension details are annotated in Fig. S8. Note that the dimension parameters of the fabricated MO-TENG are slightly different from those in the mathematical model due to the limited accessibility of materials and machining and assembly errors. A step-by-step tutorial for prototyping the MO-TENG is depicted in Fig. S9, including the manufacturing, assembling, and stacking processes. This tutorial showcases the simplicity of this configuration, making it easy to fabricate, integrate, and utilize in practical applications.

Material selection

This subsection investigates the influences of the triboelectrification materials on the MO-TENG. A consistent external excitation with a frequency of 0.5 Hz and a peak-to-peak amplitude of 90 mm is generated using a linear motor, as depicted in Figs. S10, 11. Figure 3a–c presents a comparative analysis of the triboelectrification potential of M-TENGs utilizing various dielectric balls. Specifically, the M-TENG using PTFE balls demonstrates superior performance, with an open-circuit voltage (V_{oc}) of 1628.34 V, a short-circuit current (I_{sc}) of 306.89 nA, and a short-circuit charge (Q_{sc}) of 147.9 nC. Polypropylene
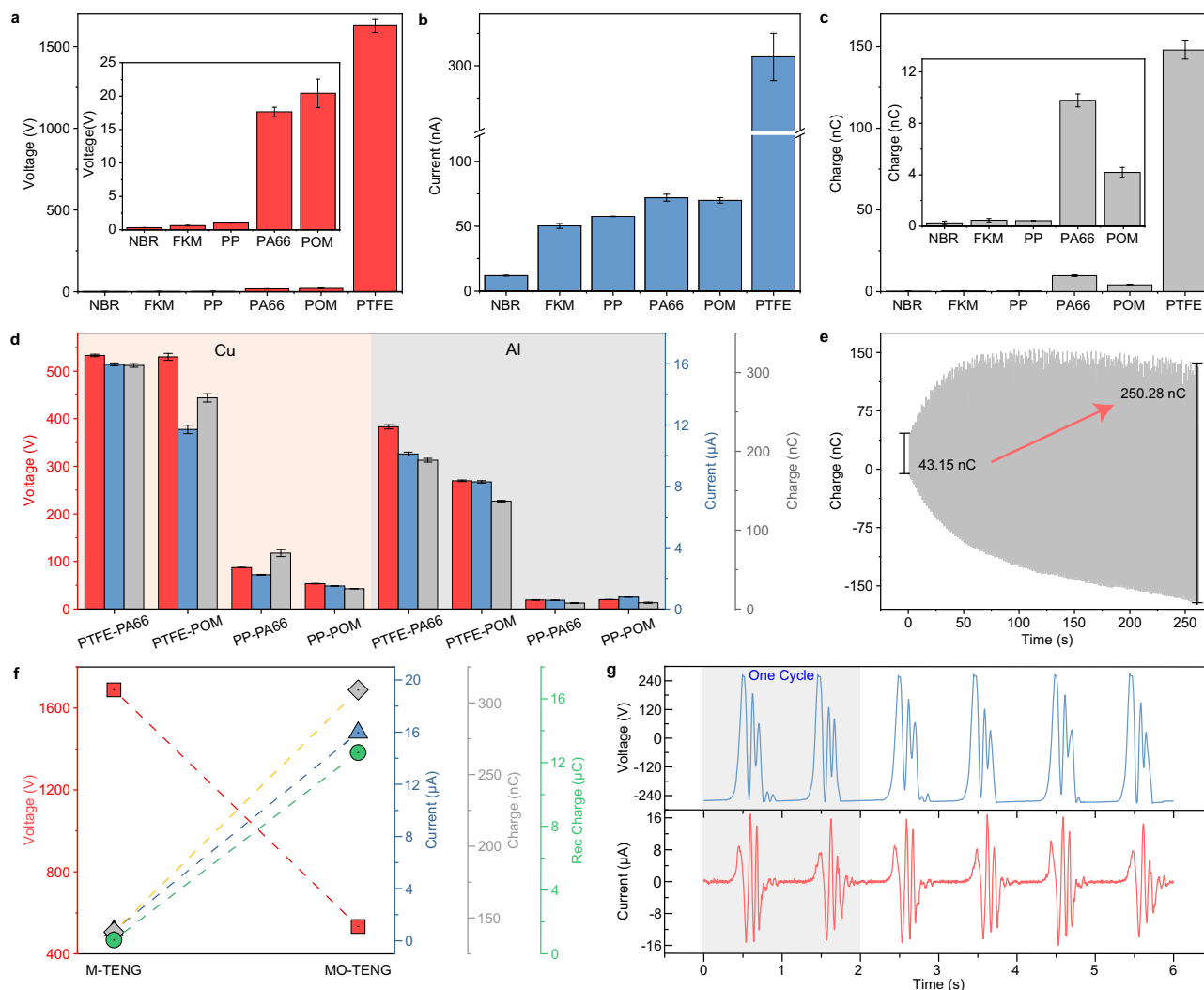
Fig. 3 | Material selection of the MO-TENG. a–c V_{oc}, I_{sc}, and Q_{sc} of the M-TENG using different materials. Data are presented as mean values ± SD. **d** Output performance of MO-TENGs using different material combinations. Data are presented as mean values ± SD. **e** Charge accumulation process of the MO-TENG. **f** Output comparison between the M-TENG and the MO-TENG. **g** Voltage and current waveforms of the MO-TENG.

(PP) balls, Polyoxymethylene (POM) balls, and Nylon (PA66) balls can also be considered, although their outputs are smaller. Nitrile butadiene rubber balls and fluoroelastomer balls produced negligible outputs and were, thus, not considered. According to the triboelectric series, PTFE and PP exhibit high affinities to attract electrons, whereas POM and PA66 are more prone to lose electrons[21,40,44]. For the MO-TENG, which employs the ternary electrification architecture, it is crucial to use two types of dielectric balls with opposite triboelectrification properties. Furthermore, a third material is required to serve as the electrode and form the ternary electrification architecture. Aluminum (Al) and Cu are often used as electrode materials. We tested eight different combinations of these materials to evaluate and compare the performance. As can be found in Fig. 3d, for identical dielectric balls, the MO-TENG using Cu as the electrode material generates a higher output than those using Al. Among all combinations, the one comprising [PTFE, PA66, Cu] exhibits the highest performance. Therefore, it is identified as the optimal combination for further investigation in subsequent studies.

Leveraging on the opposite-charge-enhancement mechanism, the Q_{sc} witnesses a significant rise from 43.15 to 250.28 nC during the rolling cycle in 260 s, as shown in Fig. 3e and Fig. S12. Figure 3f and Fig. S13 present and compare the outputs of the M-TENG and MO-TENG. The I_{sc}, Q_{sc}, and rectified charge experience substantial growth

from 0.77 to 15.96 μA, 140.17 to 308.95 nC, and 0.87 to 12.63 μC (in 5 s), respectively. Nevertheless, the V_{oc} exhibits a notable reduction, decreasing from 1688.16 V (M-TENG) to 532.94 V (MO-TENG). This phenomenon is attributed to the increase of the capacitance of the TENG, which results from the introduction of grating electrodes, as revealed in Fig. S14. According to Eq. (5), an increase in capacitance will result in a voltage drop[36].

$$V_{oc} = \frac{\triangle\sigma_{sc} \cdot S}{C} \qquad (5)$$

where $\triangle\sigma_{sc}$ is the short-circuit transferred charge density, S is the total electrode area, and C is the capacitance between the electrodes. Figure 3g presents the voltage and current waveforms of the MO-TENG over a duration of 6 s. Gray-shaded areas emphasize the device's responses within one single cycle, featuring 6 voltage peaks and 12 current peaks (details are depicted in Fig. S15). This configuration results in an increased charge transfer speed and, thus, a larger current output, underscoring the MO-TENG's enhanced performance.

Performance evaluation

This subsection presents the analysis of the output performance of the MO-TENG. As illustrated in Fig. S16, the MO-TENG is mounted on a
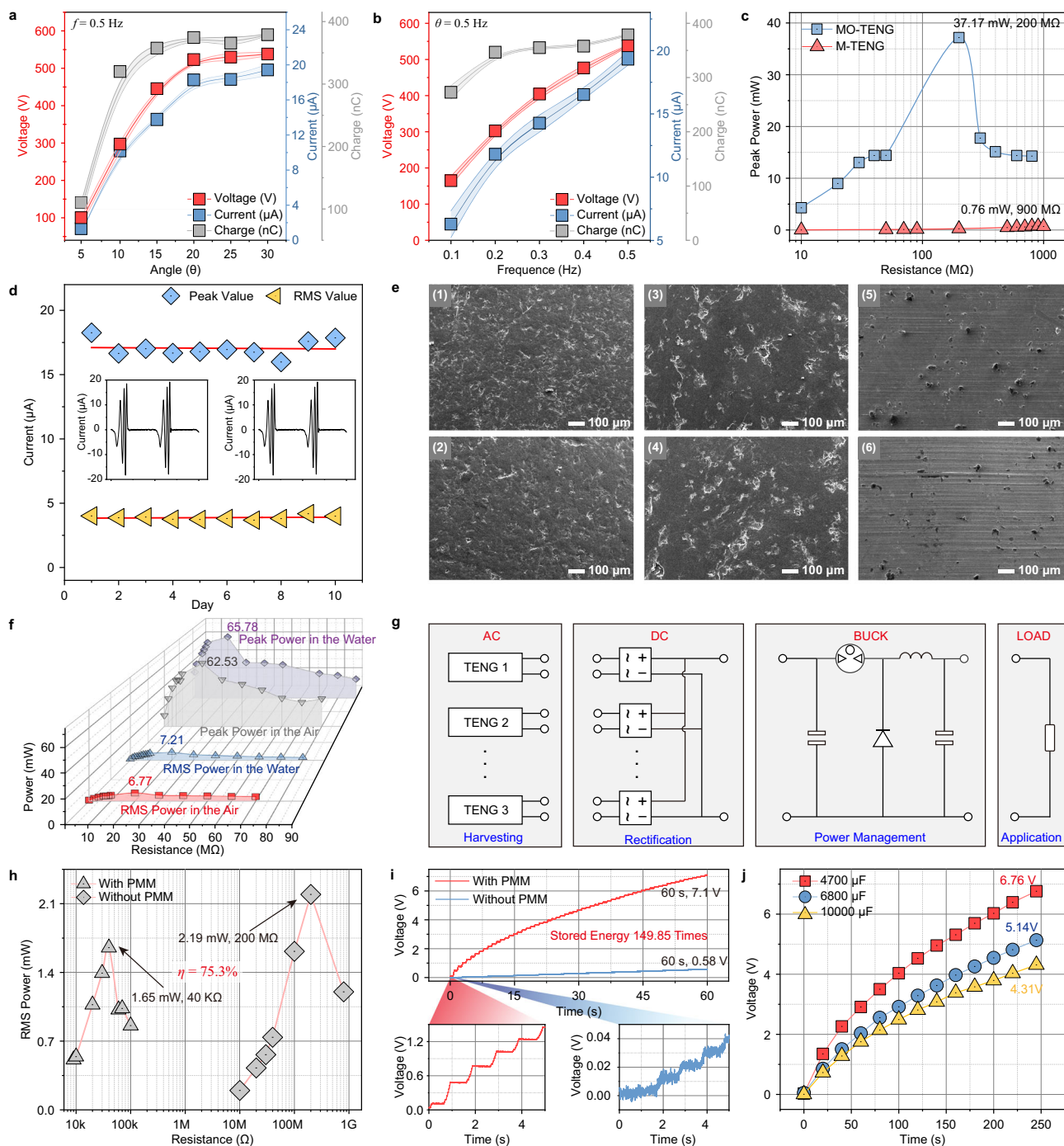
Fig. 4 | Output performance of the MO-TENG. a, b The output of the MO-TENG under excitations with various swing angles and frequencies. Data are presented as mean values ± SD. **c** Peak power comparison of the MO-TENG and M-TENG. **d** Durability test of the MO-TENG. **e** SEM images of the unused PTFE ball, Nylon ball, and Cu (sub-graphs in the first row: 1, 3, 5) and the used ones after 10 days (sub-graphs in the second row: 2, 4, 6). **f** The resistance dependence of the peak and RMS power of the stacked 10 MO-TENG units excited by the swing platform and regular wave. **g** Circuit diagram of the PMM. **h** The resistance dependence of the RMS power of a single MO-TENG unit using and without using PMM. **i** Comparison of the capacitor (100 μF) charging speeds of the MO-TENG using and without using PMM. **j** The charging histories of stacked MO-TENGs (10 units) using PMM for different capacitors.

rocking platform, which is controlled by a stepper motor to simulate wave excitation by varying the swing angle (θ) and the frequency of the rocking motion (f). As depicted in Fig. 4a, with f set at 0.5 Hz and θ varying between 5° and 30°, the open-circuit voltage (V_{oc}) generated by the MO-TENG rises from 100.36 to 538.15 V. At the same time, I_{sc} increases from 1.31 to 19.42 μA, and the short-circuit charge Q_{sc} from 110.32 to 379.06 nC. The MO-TENG's performance improves with a larger θ because the triboelectrification effect gets enhanced when the

dielectric balls roll over longer distances under a larger excitation. By maintaining θ at 30°, the impacts of the excitation frequency f (varied from 0.1 to 0.5 Hz) on V_{oc}, I_{sc}, and Q_{sc} are presented in Fig. 4b. As the red dot line shows, increasing the frequency from 0.1 to 0.5 Hz results in V_{oc} rising from 164.84 to 537.74 V. The induction charge transfer speed rises with the increase of the excitation frequency, resulting in a surge in the current output from 6.27 to 19.37 μA. The transfer charge Q_{sc} also exhibits a rising trend, increasing from 272.77 to 378.68 nC,

when f increases from 0.1 to 0.5 Hz. This phenomenon occurs as a higher excitation frequency prompts the balls to traverse more swiftly, thereby converting more kinetic energy into electricity. The raw data waveforms of the voltage, current, and transfer charge of the MO-TENG and the corresponding RMS current values are presented in Figs. S17–22. Previous research shows that V_{oc} and Q_{sc} tend to saturate when the swing angle and excitation frequency are tuned high enough[25,33]. Considering the real ocean waves, the parameters are limited to a certain range ($\theta < 30°$, $f < 0.5$ Hz). Across those figures, it can be observed that, with the increases in the swing angle and excitation frequency, the growth rates of V_{oc} and Q_{sc} gradually decline.

By varying the load resistance while keeping the θ and the f constant at 30° and 0.5 Hz, respectively, the power output of the MO-TENG is investigated. As depicted in Fig. 4c and Fig. S23, the MO-TENG achieves the maximum instantaneous power output of about 37.17 mW at an optimal resistance of 200 MΩ. Compared to the M-TENG, which reaches the maximum instantaneous power of 0.76 mW at the matching resistance of 900 MΩ, the MO-TENG's maximum instantaneous power output is about 48.9 times higher, and its internal resistance is reduced by ~3.5-folds. With an RMS power of about 2.19 mW, the MO-TENG outperforms the M-TENG by more than 23 times, as shown in Fig. S24. According to the geometries in Fig. S8, the volume of the MO-TENG is determined to be 400.98 cm³. Hence, the instantaneous and RMS power densities are 185.4 and 10.92 W/(m³·Hz), respectively. These results highlight the MO-TENG's unparalleled performance among wave energy harvesting TENGs that utilize diverse mechanisms. A comprehensive comparison is detailed in Fig. 1f, Fig. S25, and Table S1, showcasing the MO-TENG's superior output.

The abrasion issue that inevitably occurs on the contact interface seriously deteriorates TENG's performance[37]. The inherent low-friction nature of the rolling mode can help maintain the TENG's stable output over a prolonged period, enhancing its durability in marine environments. As depicted in Fig. 4d, the MO-TENG generates a consistently stable current output over 10 days. The insets within Fig. 4d illustrate the current waveforms recorded on days 1 and 10, proving the MO-TENG's long-term operational reliability. Moreover, Fig. 4e displays scanning electron microscopic (SEM) images of the surfaces of the PTFE ball, Nylon ball, and Cu film before use (sub-images 1, 3, and 5 in the first row) and after 10 days of testing (sub-images 2, 4, and 6 in the second row). The minimal interface abrasion observed upon comparison substantiates the MO-TENG's stable output and high durability.

Since one single MO-TENG unit has a limited output, multiple MO-TENG units can be stacked and connected in parallel to boost the output and lower the internal resistance. The resistance dependence of the peak and RMS power outputs of a stacked MO-TENG having 10 units are shown in Fig. 4f and Figs. S26, 27. It was tested on a three-degree-of-freedom (3-DOF) swing platform (Fig. S28) and in a wave tank (Fig. S29). This approach offers a practical solution to meet the power requirements of various electronic devices. However, one issue with the stacked configuration is that the asynchronous movements of the inertial balls across different layers may lead to the neutralization of current, thereby reducing the overall effectiveness. To address this challenge, we have developed a PMM, to mitigate these adverse effects and maximize the power output. The circuit diagram and other details are shown in Fig. 4g and the "Methods" section. As depicted in Fig. 4h, the RMS power outputs of a single MO-TENG unit using PMM and without using PMM are evaluated. Under the excitation of 0.5 Hz and 30°, the RMS power is 1.65 mW at a low optimal resistance of 40 KΩ when using PMM, and it is 2.19 mW at 200 MΩ without using PMM. Thus, the energy efficiency of the PMM is about 78.5%, calculated using the following equation: $\eta = P_{RMS,with\ PMM}/P_{RMS,without\ PMM}$. Despite the decline of the RMS power, the significant decrease in internal resistance due to the use of PMM will facilitate impedance matching and enhance charging speed. As shown in Fig. 4i, a single MO-TENG unit using PMM can collect 149 times more energy when

charging a capacitor (100 μF) in 1 min. The charging data in the initial 5 s show that after using PMM, the charging curve exhibits a step-like increase, signifying a high growth rate. Figure S30 and Fig. 4j illustrate the charging performance of a single MO-TENG unit and ten stacked MO-TENG units using PMM for other large capacitors. These results indicate that the stacked MO-TENGs have significant potential to serve as power sources for heavy-load electronic devices.

Application demonstration

Ten MO-TENG units are stacked to demonstrate the application in the marine environment. Figure 4g shows the circuit design for the stacked MO-TENG (physical prototype shown in Fig. 5a). When subjected to the excitation of the commercial swing platform at 0.5 Hz and 10°, the stacked MO-TENG units can easily illuminate 120 LEDs (0.5 W) connected in series, as shown in Fig. 5b and Supplementary Movie 1. Notably, supplying power to sensors is a pivotal application scenario for TENGs toward self-powered IoT nodes. Nevertheless, the wave excitation changes unpredictably over time. The power consumption of sensors and wireless transmitter modules is typically several to several tens of times higher than the power outputs of TENGs[27]. Hence, the harnessed energy from MO-TENGs needs to be carefully regulated to realize self-powered marine in-situ monitoring. The vital problem is that if the capacitor prematurely provides energy to the rest of the electronic components, it would drain the stored energy and hardly meet the end. To prevent premature power-up of the wireless sensing circuit, we added a cold-start phase and developed an SOS system by synergizing energy harvesting, sensing, and wireless communication techniques. The architecture of the SOS system is shown in Fig. 5c, and details of the electronics and workflow are described in the "Methods" section.

Considering the excellent charging performance of the stacked MO-TENG units and the relatively high energy consumption of the SOS system, a large storage capacitor C_2 of 6800 μF is used. We studied the performance of the SOS system under an external excitation by the linear motor. As shown in Fig. 5d and Supplementary Movie 2, the self-powered SOS system accomplished the sensing task three times in the recorded time window. The time-history chart of the storage capacitor (C_2) voltage is illustrated in Fig. 5e. Under the external excitation, the SOS achieved a cold-start at 244 s, with the capacitor C_2 being charged from 0 to 5.10 V. Then, the SOS system realized a quick wake-up, and power was delivered to the total dissolved solids (TDS) sensor and LoRa module for collecting and sending data, as shown in Fig. 5f. This process continued for about 1.5 s and ended with a voltage drop of 1.4 V, which indicates a release of 41.9 mJ of energy. Then, all appliances stopped working except LTC3588-1, and the under-voltage lockout (UVLO) function restarted to guarantee the energy accumulation of the capacitor (Fig. 5g).

We sealed the stacked MO-TENG together with the circuit module in an acrylic buoy to investigate its application potential in the marine environment. As demonstrated in Fig. S31 and Supplementary Movie 3, under the excitation of the simulated wave (0.6 Hz, 8 cm height), the buoy with the 10 stacked MO-TENG units can directly power a marine navigation light. Moreover, as shown in Fig. 5h, i and Supplementary Movie 4, the self-powered buoy collects and transmits the TDS value to the receiving end three times within 150 s. Considering the random nature (frequency, direction, etc.) of real waves, the buoy is driven to conduct movements in all 6-DOF: surge/sway/heave, roll/pitch/yaw. The external excitation direction does not always align with the multi-tunnel's orientation, and an angle often exists between them. As illustrated in Fig. S32, α is designated as the angle between the external excitation direction and the tunnel orientation. Figure S33 shows how α impacts the output of a stacked MO-TENG with 10 units under an excitation of 0.5 Hz and a 10° generated by the 3-DOF platform. The results reveal that the stacked MO-TENGs achieve optimal output performance when α is at 0°. As α increases, both I_{sc} and Q_{sc} exhibit a
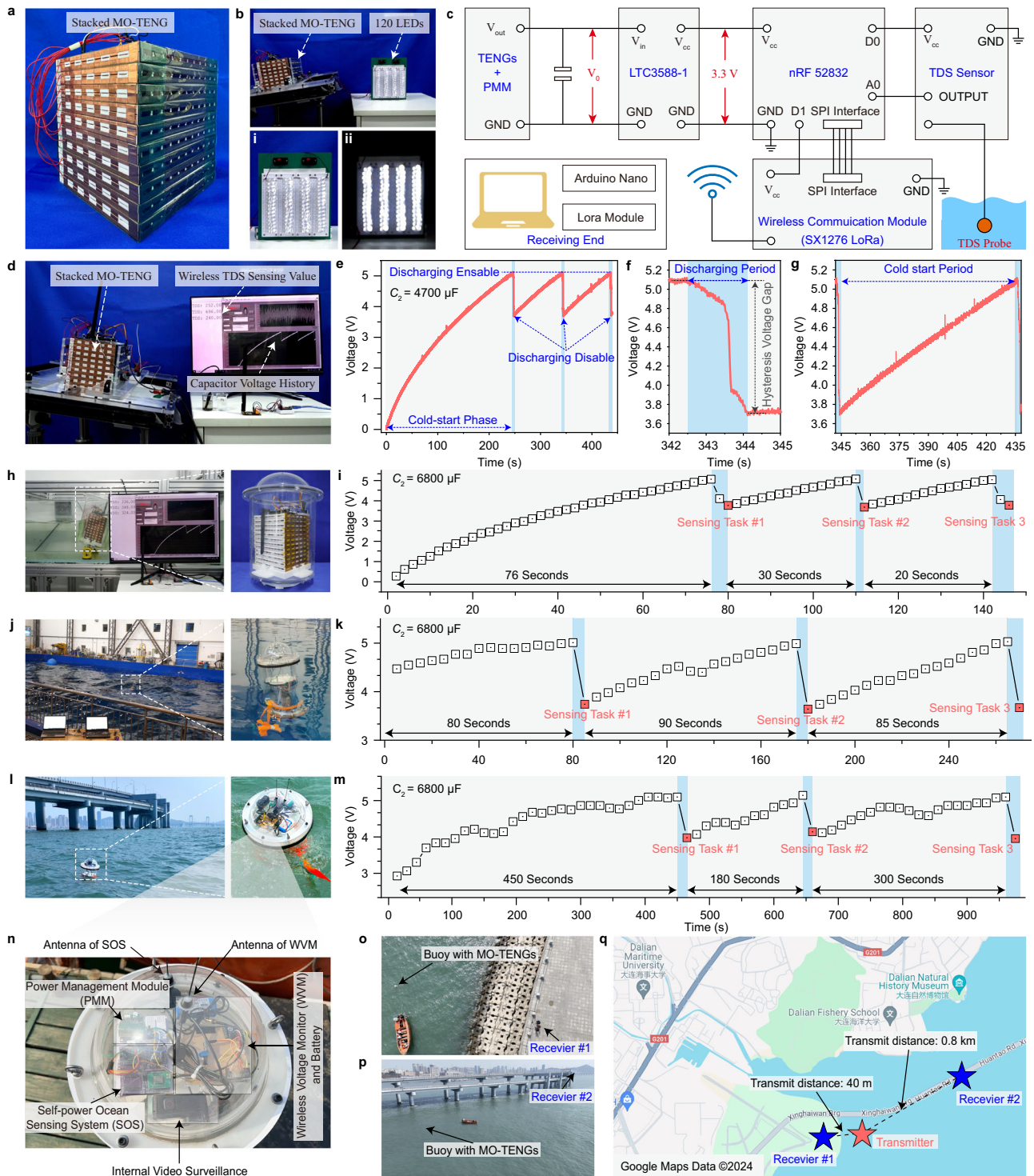
Fig. 5 | Application demonstration of the MO-TENG. a Photograph of the stacked MO-TENGs (10 units). **b** Using the stacked MO-TENGs to light up 120 LEDs. The sub-figures show the application under light conditions (i) and dark conditions (ii), respectively. **c** Architecture of the SOS system. **d** Self-powered water quality sensing test excited by a 3-DOF platform. **e–g** Voltage history of the capacitor in the self-powered sensing process. Photographs and voltage histories of the self-powered sensing process in the regular wave tank (**h, i**), random wave tank (**j, k**), and real ocean environment (**l, m**). **n** Illustration of different functional parts in the dome of the buoy. **o, p** The location arrangement of the receiver and the buoy (transmitter). **q** The illustration of the transmission distance of the SOS system.

gradual decline. Upon reaching an angle of 90°, the output diminishes to almost zero.

To address this, we designed a buoy with 30 cells and organized into groups of 10 cells each. Each group is twisted at an angle of 120° to collect wave energy from different directions efficiently. The buoy is designed to be 1.0 m high with a diameter of 0.28 m, and detailed

dimensions are annotated in Fig. S34. The capsule-shaped buoy was weighted down (using iron blocks positioned near its base) to achieve a draft of 0.6 m and maintain a vertical center of gravity (VCG) located 0.25 m above the baseline. The buoy is loosely moored with a single catenary cable and a gravity anchor, and the design details are shown in Supplementary Note 2. To analyze the data and validate the working

state, a wireless voltage monitor (WVM) was designed to collect the voltage values of the storage capacitor and transmit the data via a LoRa wireless communication module. The WVM is powered by a Li-ion battery, which is isolated from the MO-TENG and SOS system. The buoy, equipped with 30 MO-TENGs units and other components, is depicted in Fig. S35. A random wave tank ($50 \times 30 \times 5$ m), as shown in Fig. S36, was used to test the energy harvesting capability and self-powered sensing performance of the buoy. In Fig. 5j, k and Supplementary Movie 5, the buoy powered by the stacked MO-TENG successfully transmitted the TDS value three times via LoRa communication under a random wave excitation. The energy harvesting process took 80, 90, and 85 s, respectively, for each transmission.

Furthermore, as illustrated in Fig. 5l, the buoy equipped with stacked 30 MO-TENG units was deployed in the real ocean environment of Bohai Bay, Dalian City, to showcase its potential for practical use. The auxiliary functional circuit modules were housed within the buoy's dome, as depicted in Fig. 5n. In Figure S37 and Supplementary Movie 6, the buoy recharged the capacitors by harnessing energy from the wave and enabled the SOS system to realize a cold start after 450 s. This self-powered smart buoy successfully detected the water quality and transmitted the data via the SOS system. The mission was carried out three times to prove the robustness, and the charging history is displayed in Fig. 5m. Receiver #1 and receiver #2 received the wireless water quality sensing signals at a distance of 40 m and 0.8 km from the buoy, respectively, as shown in Fig. 5o–q. This proves that the smart buoy can be deployed along the coast and marks a pioneering endeavor to use a fully TENG-based device for realizing self-powered sensing applications under actual ocean conditions.

Discussion

In this work, we have designed and prototyped a rolling-mode triboelectric nanogenerator (MO-TENG) with enhanced performance by adopting the strategies of multi-tunnel grating electrodes and opposite-charge-enhancement. The effective electrode area enlargement by the multi-tunnel design has been explained. Comprehensive studies of the working principle and performance of the proposed MO-TENG have been presented. Benefiting from this design, the MO-TENG can produce an instantaneous power density of 185.4 W/(m³·Hz) and an RMS power density of 10.92 W/(m³·Hz). A PMM has been developed to enhance the output of the stacked MO-TENGs, leading to a 150-fold increase in energy storage. Furthermore, an SOS system featuring cold-start capability has been developed for remote and wireless water quality monitoring. At the same time, stacked MO-TENGs enable the scalable construction of self-powered nodes for maritime applications, and this has been validated under various laboratory conditions. Furthermore, a buoy equipped with stacked MO-TENGs was tested in a real ocean environment for powering the SOS system. The intelligent buoy accomplished the self-powered sensing task three times within 920 s over a maximum transmission distance of 0.8 km, which marks the pioneering instance of a TENG-powered device serving in a real ocean environment. The results have validated the superiority of the MO-TENG and proven its potential as the cornerstone for the self-powered sensing nodes that serve the marine IoT and the ocean digital twin.

Methods

Fabrication of the MO-TENG
One MO-TENG unit is made up of two substrates, two baffles, one pair of electrodes, and dielectric balls. The assembly process involves the following steps: (1) fabricate the substrates and baffles using an FDM 3D printer (Bambu X1 Carbon), utilizing PLA as the material. (2) Affix Cu tapes onto the substrates, ensuring a consistent gap and connecting them at regular intervals to create a pair of grating electrodes. (3)

Load the dielectric balls into the tunnel. (4) Complete the assembly by adding the two baffles and the second substrate, securing everything in place with Kapton tape. Dimension details and a step-by-step tutorial of the MO-TENG can be found in Figs. S8 and S9.

Components of the PMM circuit
The PMM comprises two parts: the rectification part and the buck part. The rectification part regulates the AC outputs of the stacked MO-TENGs and converts them to DC through the full-bridge rectifier (DB-107). The core of the PMM is the buck part that can adjust the voltage and the impedance of the MO-TENG[45]. A capacitor C_1 of 100 pF is the direct load of the harvester to extract maximum energy during the charging period. A gas discharge tube (SX51-230) acts as a switch, enabling C_1 to accumulate energy under low-frequency excitations and release it instantaneously. The rest of the buck part consists of an ultrafast diode D (MUR460) and an inductor L (1 mH).

Components of the self-powered ocean sensing (SOS) system
SOS comprises the stacked MO-TENG units, the PMM, a charging capacitor C_2, a voltage regulator (LTC3588-1), a low-power consumption system on chip (nRF 52832), a long-distance communication module (Lora, SX1276), a water quality sensor to detect the value of TDS, and a receiving end (consisting of an Arduino Nano, a Lora module and a laptop). The capacitor C_2 collects the electricity from the stacked MO-TENG units through PMM and connects the voltage regulator. The voltage regulator, LTC3588-1, features an ultra-low quiescent current UVLO mode with a hysteresis window of -1 V. This design ensures that the system can quickly cold start once sufficient energy is collected in the storage capacitor and remains operational even if the voltage drops within a tolerance[46,47].

Fabrication of the buoys
The diameter and height of the acrylic buoy in Fig. 5h are 25 and 40 cm, respectively. The buoy top was sealed with a rubber O-ring. Before the water tank test, the MO-TENGs, PMM, and SOS systems were sealed inside the buoy. The TDS sensor probe was positioned outside the buoy, connected by a wire that passes through the buoy bottom, which was sealed with a waterproof joint. The acrylic buoy depicted in Fig. 5i, j has a diameter of 28 cm and a height of 104 cm. Dimension details are shown in Fig. S34.

Characterization and measurement
A Keithley 6514 electrometer was used to measure the charge transfer characteristic of the MO-TENG, which was displayed in a custom Lab-VIEW VI application. A linear motor (Linmot E1100) (Figs. S10, 11) and a stepper motor-enabled swing platform (Fig. S16) were utilized to simulate simple excitations to help evaluate the output performance of the MO-TENG. A 3-DOF swing platform was used to stimulate swing excitation (Fig. S28). A wave tank ($40 \times 40 \times 240$ cm³) was designed to simulate regular wave excitations (Fig. S29). A random wave tank was used to simulate the random wave condition in a real ocean environment (Fig. S36).

The peak/instantaneous power and the RMS power values are calculated through $P_{\text{peak/RMS}} = I_{\text{peak/RMS}}^2 \cdot R$, where I_{peak} and I_{RMS} represent the peak and RMS values of the harvester's current output, respectively. R is the optimal resistance of the harvester. The peak/RMS power density values are calculated through $\frac{P_{\text{peak}}/P_{\text{RMS}}}{\text{Volume} \cdot \text{Frequency}}$, where "Volume" specifies the dimensions of the energy harvester and "Frequency" corresponds to the excitation state.

In the random wave tank and actual ocean test, a wireless voltage sensing platform, along with other components, was sealed in the buoy to monitor and transmit the real-time voltage values of the storage capacitor (Fig. 5n). The platform consisted of an Arduino Nano, a voltage sensor, and a LoRa wireless communication module (SX1276).

Data availability

The Source data generated in this study are provided in the Supplementary Information. Any additional requests for information can be directed to and will be fulfilled by the corresponding authors. Source data are provided with this paper.

References

1. Collins, M. et al. The impact of global warming on the tropical Pacific Ocean and El Niño. *Nat. Geosci.* **3**, 391–397 (2010).
2. Jepsen, E. M. & De Bruyn, P. J. N. Pinniped entanglement in oceanic plastic pollution: a global review. *Mar. Pollut. Bull.* **145**, 295–305 (2019).
3. Wang, Y. et al. Highly adaptive triboelectric-electromagnetic hybrid nanogenerator for scavenging flow energy and self-powered marine wireless sensing. *Adv. Mater. Technol.* **8**, 2201245 (2023).
4. Wang, Y. et al. Flexible seaweed-like triboelectric nanogenerator as a wave energy harvester powering marine Internet of Things. *ACS Nano* **15**, 15700–15709 (2021).
5. Yang, H., Wang, H., Ma, Y. & Xu, M. Prediction of wave energy flux in the Bohai Sea through automated machine learning. *J. Mar. Sci. Eng.* **10**, 1025 (2022).
6. Yang, H., Wang, H., Gao, Y., Liu, X. & Xu, M. A significant wave height forecast framework with end-to-end dynamic modeling and lag features length optimization. *Ocean Eng.* **266**, 113037 (2022).
7. Wang, H. & Falzarano, J. Efficient assessment for the pitchpoling risks of a generic wave energy converter based on first passage statistics. *Ocean Eng.* **257**, 111619 (2022).
8. Ahmed, A. et al. Design of an S-shaped point-absorber wave energy converter with a non-linear PTO to power the satellite-respondent buoys in the East China Sea. *Ocean Eng.* **275**, 114162 (2023).
9. Li, Z. et al. Towards real-time self-powered sensing with ample redundant charges by a piezostack-based frequency-converted generator from human motions. *Energy Convers. Manag.* **258**, 115466 (2022).
10. Li, Z., Peng, X., Hu, G. & Peng, Y. Theoretical, numerical, and experimental studies of a frequency up-conversion piezoelectric energy harvester. *Int. J. Mech. Sci.* **223**, 107299 (2022).
11. Hu, G., Zhao, C., Yang, Y., Li, X. & Liang, J. Triboelectric energy harvesting using an origami-inspired structure. *Appl. Energy* **306**, 118037 (2022).
12. Zhao, C. et al. Wide-bandwidth triboelectric energy harvester combining impact nonlinearity and multi-resonance method. *Appl. Energy* **348**, 121530 (2023).
13. Yu, H. et al. High performance additional mass enhanced film structure triboelectric nanogenerator for scavenging vibration energy in broadband frequency range. *Nano Energy* **107**, 108182 (2023).
14. Wang, Z. L. Entropy theory of distributed energy for internet of things. *Nano Energy* **58**, 669–672 (2019).
15. Fan, F.-R., Tian, Z.-Q. & Lin Wang, Z. Flexible triboelectric generator. *Nano Energy* **1**, 328–334 (2012).
16. Zhai, H., Ding, S., Chen, X., Wu, Y. & Lin Wang, Z. Advances in solid–solid contacting triboelectric nanogenerator for ocean energy harvesting. *Mater. Today* **65**, 166–188 (2023).
17. Wang, H., Xu, L. & Wang, Z. Advances of high-performance triboelectric nanogenerators for blue energy harvesting. *Nanoenergy Adv.* **1**, 32–57 (2021).
18. Cheng, T., Shao, J. & Wang, Z. L. Triboelectric nanogenerators. *Nat. Rev. Methods Prim.* **3**, 39 (2023).
19. Zhu, G. et al. Harvesting water wave energy by asymmetric screening of electrostatic charges on a nanostructured hydrophobic thin-film surface. *ACS Nano* **8**, 6031–6037 (2014).
20. Kim, T. et al. Direct-current triboelectric nanogenerator via water electrification and phase control. *Nano Energy* **52**, 95–104 (2018).
21. Yuan, Z. et al. Spherical triboelectric nanogenerator with dense point contacts for harvesting multidirectional water wave and vibration energy. *ACS Energy Lett.* **6**, 2809–2816 (2021).
22. Cheng, P. et al. Largely enhanced triboelectric nanogenerator for efficient harvesting of water wave energy by soft contacted structure. *Nano Energy* **57**, 432–439 (2019).
23. Wu, H., Wang, Z. & Zi, Y. Multi-mode water-tube-based triboelectric nanogenerator designed for low-frequency energy harvesting with ultrahigh volumetric charge density. *Adv. Energy Mater.* **11**, 2100038 (2021).
24. Zhao, L., Zou, H., Xie, X., Guo, D. & Gao, Q. Mechanical intelligent wave energy harvesting and self-powered marine environment monitoring. *Nano Energy* **108**, 108222 (2023).
25. Wang, H. et al. A stackable triboelectric nanogenerator for wave-driven marine buoys. *Nanomaterials* **12**, 594 (2022).
26. Zhang, S. L. et al. Rationally designed sea snake structure based triboelectric nanogenerators for effectively and efficiently harvesting ocean wave energy with minimized water screening effect. *Nano Energy* **48**, 421–429 (2018).
27. Zhao, T. et al. Recent progress in blue energy harvesting for powering distributed sensors in ocean. *Nano Energy* **88**, 106199 (2021).
28. Xu, R., Wang, H., Xi, Z., Wang, W. & Xu, M. Recent progress on wave energy marine buoys. *J. Mar. Sci. Eng.* **10**, 566 (2022).
29. Liu, L. et al. Nodding duck structure multi-track directional freestanding triboelectric nanogenerator toward low-frequency ocean wave energy harvesting. *ACS Nano* **15**, 9412–9421 (2021).
30. Yang, X. et al. Macroscopic self-assembly network of encapsulated high-performance triboelectric nanogenerators for water wave energy harvesting. *Nano Energy* **60**, 404–412 (2019).
31. Wang, X. et al. Triboelectric nanogenerator based on fully enclosed rolling spherical structure for harvesting low-frequency water wave energy. *Adv. Energy Mater.* **5**, 1501467 (2015).
32. Zhang, Z. et al. Multi-tunnel triboelectric nanogenerator for scavenging mechanical energy in marine floating bodies. *J. Mar. Sci. Eng.* **10**, 455 (2022).
33. Wang, H. et al. Sandwich-like triboelectric nanogenerators integrated self-powered buoy for navigation safety. *Nano Energy* **84**, 105920 (2021).
34. Xu, M. et al. High power density tower-like triboelectric nanogenerator for harvesting arbitrary directional water wave energy. *ACS Nano* **13**, 1932 (2019).
35. Li, X. et al. Three-dimensional chiral networks of triboelectric nanogenerators inspired by metamaterial's structure. *Energy Environ. Sci.* **16**, 3040–3052 (2023).
36. Xie, Y. et al. Grating-structured freestanding triboelectric-layer nanogenerator for harvesting mechanical energy at 85% total conversion efficiency. *Adv. Mater.* **26**, 6599–6607 (2014).
37. Wu, H., Wang, S., Wang, Z. & Zi, Y. Achieving ultrahigh instantaneous power density of 10 MW/m^2 by leveraging the opposite-charge-enhanced transistor-like triboelectric nanogenerator (OCT-TENG). *Nat. Commun.* **12**, 5470 (2021).
38. Duan, Y. et al. Scalable rolling-structured triboelectric nanogenerator with high power density for water wave energy harvesting toward marine environmental monitoring. *Nano Res.* **16**, 11646–11652 (2023).
39. Jing, Z. et al. 3D fully-enclosed triboelectric nanogenerator with bionic fish-like structure for harvesting hydrokinetic energy. *Nano Res.* **15**, 5098–5104 (2022).
40. Wang, Z. L. & Wang, A. C. On the origin of contact-electrification. *Mater. Today* **30**, 34–51 (2019).
41. Wang, Z. L., Lin, L., Chen, J., Niu, S. & Zi, Y. *Triboelectric Nanogenerators*. (Springer Cham, 2016). https://doi.org/10.1007/978-3-319-40039-6.

42. Deng, W. et al. Ternary electrification layered architecture for high-performance triboelectric nanogenerators. *ACS Nano* **14**, 9050–9058 (2020).
43. Lin, L. et al. Robust triboelectric nanogenerator based on rolling electrification and electrostatic induction at an instantaneous energy conversion efficiency of ~55. *ACS Nano* **9**, 922–930 (2015).
44. Zou, H. et al. Quantifying the triboelectric series. *Nat. Commun.* **10**, 1427 (2019).
45. Fu, X. et al. Breeze-wind-energy-powered autonomous wireless anemometer based on rolling contact-electrification. *ACS Energy Lett.* **6**, 2343–2350 (2021).
46. Li, X. et al. ViPSN: A Vibration-Powered IoT Platform. *IEEE Internet of Things Journal* **8**, 1728–1739 (2021).
47. Li, X., Tang, H., Hu, G., Zhao, B. & Liang, J. ViPSN-Pluck: A Transient-Motion-Powered Motion Detector. *IEEE Internet of Things Journal* **9**, 3372–3382 (2022).

Acknowledgements

Author contributions

G.H., H.W., and M.X. supervised and guided the project; Y.W., H.D., H.Y. (Hengyi YANG), and Z.X. conceived the idea and designed the experiments. C.Z. and Z.Q. optimized the TENG's configuration and manufacturing methods; Y.W., H.D., H.Y. (Hongyong YU), Z.X., X.P., H.Y.(Hongyong YU), and Y.Z. fabricated the harvester and performed the experiments; X.C. and X.L. designed and fabricated the auxiliary circuits.

Competing interests

The authors declare no competing interests.

Additional information

Supplementary information The online version contains supplementary material available at https://doi.org/10.1038/s41467-024-51245-5.

Correspondence and requests for materials should be addressed to Guobiao Hu, Hao Wang or Minyi Xu.

Peer review information *Nature Communications* thanks Van-Tien Bui, Suan Hui Pu, and the other, anonymous, reviewer(s) for their contribution to the peer review of this work. A peer review file is available.

Reprints and permissions information is available at http://www.nature.com/reprints

Publisher's note Springer Nature remains neutral with regard to jurisdictional claims in published maps and institutional affiliations.